Ab initio Spin-Mapping Non-adiabatic Dynamics Simulations of Photochemistry

Braden M. Weight,[1, a)] Arkajit Mandal,[2] Deping Hu,[3] and Pengfei Huo[4, 5, b)]

[1)] *Department of Physics and Astronomy, University of Rochester, Rochester, NY 14627, U.S.A.*

[2)] *Department of Chemistry, Columbia University, New York, NY, 10027, U.S.A.*

[3)] *Center for Advanced Materials Research, Beijing Normal University, Zhuhai 519087, China*

[4)] *Department of Chemistry, University of Rochester, Rochester, NY 14627, U.S.A.*

[5)] *The Institute of Optics, Hajim School of Engineering, University of Rochester, Rochester, New York, 14627*

We perform on-the-fly non-adiabatic molecular dynamics simulations using the recently developed spin-mapping formalism. Two quantum dynamics approaches based on this mapping formalism, (i) the fully linearized spin-LSC and (ii) the partially linearized spin-PLDM, are explored using the quasi-diabatic propagation scheme. We have performed dynamics simulations in four *ab initio* molecular models for which benchmark *ab initio* multiple spawning data has been published. We find that the spin-LSC approach routinely outperforms the spin-PLDM approach and yields a roughly equivalent accuracy to the previously reported symmetric quasi-classical approach. We further explore the underpinnings of the spin-PLDM correlation function by decomposing its various contributions stemming from its summation over all the terms, N^2, in the density matrix-focused initial conditions where N is the number of states in the quantum subsystem. Finally, we found an approximate form of the spin-PLDM correlation function that simplifies the simulation and reduces the computational costs from N^2 to N.

I. INTRODUCTION

The simulation of realistic molecules using on-the-fly dynamics techniques has been the topic of much work over the last few decades.[1–28] Performing on-the-fly dynamics requires two major components: (i) accurate electronic structure and (ii) propagation of the correlated electron-nuclear dynamics.[29] Due to the size of the total Hilbert space needed to perform exact, full-dimensional quantum simulation, the community has resorted to various approximations. The most successful and computationally accessible methods are the mixed quantum-classical (MQC) approaches such as the fewest switches surface hopping (FSSH)[1] and the mean-field Ehrenfest approach.[30] These schemes rely on the output of electronic structure method to evolve the electronic subsystem quantum mechanically while treating the nuclear subsystem classically. Unfortunately, the MQC approximation introduces some known drawbacks, notably the breakdown of detailed balance[31], the artificial creation of electronic coherence,[18] or incorrect chemical kinetics[18]

In response to these known drawbacks, non-adiabatic dynamics approaches continue to be developed in order to systematically improve the results while retaining a similar level of computational expense. Most notably, the partial linearized density matrix[7,32] (PLDM), state-dependent ring polymer molecular dynamics[13,15,23], quantum-classical path integral (QCPI) approach[33–36], the quantum classical Liouville equation (QCLE) dynamics,[14,37] and the symmetric quasi-classical (SQC) approach[38–42] with trajectory-

specific zero-point energy.[43] Even more recently, the spin-mapping formalism has been shown to provide a substantial increase in accuracy in non-adiabatic benchmark systems, such as the Fenna-Matthew-Olson (FMO) complex, the spin-boson models,[44–47] as well as others.[48–50] Another related approach is the generalized discrete truncated Wigner approximation (GDTWA).[51] A recent connection between the popular FSSH and mapping approaches has recently been developed and tested in both model and *ab initio* settings is the mapping approach to surface hopping (MASH).[52–55]

The spin-mapping approaches build upon the idea of mapping the electronic Hilbert space to one of different types. For example, the Meyer-Miller-Stock-Thoss (MMST) mapping relations, employed, for example, in the development of the SQC[43] and PLDM[56] approaches, rely on mapping the N electronic states to that of a set of N quantum harmonic oscillators, each of which are projected to include only their ground and excited states. One of the main drawbacks of this mapping is that the Hilbert space of the quantum harmonic oscillator is larger than that of the original electronic system and so requires projection or the normalization of the population to restrict the dynamics to these DOFs. However, the spin-mapping formalism instead is able to map the electronic dynamics onto the surface of a set of spin-1/2 systems (*i.e.*, Bloch spheres) where, by construction, the normalization of the total population is guaranteed since the radius of the Bloch sphere is fixed.

In our recent works, we have developed and implemented the quasi-diabatic (QD) propagation scheme[57–63] to seamlessly combine adiabatic electronic structure methods with diabatic quantum dynamics methods. The QD scheme relies on a short-time reference nuclear geometry (whose electronic states are often called "crude

---

[a)]Electronic mail: bweight@ur.rochester.edu

[b)]Electronic mail: pengfei.huo@rochester.edu

adiabatic" states), which acts as a set of locally diabatic states during a single nuclear time-step. After this short-time propagation, the QD states are updated to the new reference geometry. In this propagation scheme, one does not construct a global diabatic representation but uses a sequence of local diabatic representations for each short-time segment to propagate quantum dynamics. Note that the quasi-diabatic propagation scheme[57–61] should not be confused with the approximate diabatic representation which is also often referred to as the "QD" representation in the literature.[64–66]

In this work, we use the QD propagation scheme to seamlessly combine the recently formulated spin-mapping quantum dynamics methods with the adiabatic output of the state-averaged complete active space complete active space self-consistent field (SA-CAS-SCF) electronic structure method. Here we perform direct on-the-fly non-adiabatic dynamics to simulate the population dynamics of various photo-excited species, ethylene, fulvene, methyliminium cation ($CH_2NH_2^+$), and 1,2-dithiane, all of which have been previously published using the higher-level, wave-packet-based *ab initio* multiple spawning (AIMS) approach.[67–69] The AIMS results are interpreted as a benchmark for the MQC results in this work. These systems provide a set of benchmarks that explore various phenomena found in non-adiabatic dynamics, such as electronic avoided crossings and conical intersections, in a simplified way and offer a direct connection between the commonly used model systems of Tully and realistic, *ab initio* molecules.[67]

Our numerical results demonstrate that the linearized spin-mapping approach outperforms the partially linearized spin-mapping (spin-PLDM) approach for all *ab initio* systems explored in this work and offers an accuracy near the same level as the SQC or FSSH approaches but with fewer *ad hoc* parameters. We further explored the nature of the spin-PLDM correlation function by examining the various components individually. Here we found that an approximate scheme can be constructed to give results of similar accuracy to the full spin-PLDM correlation function, where one only needs to calculate the upper triangle of the N^2 initial conditions including the diagonal cases. This reduces the computational expense from N^2 trajectory-converged simulations to $\frac{N(N-1)}{2}+1$ simulations, still amounting to more computations than the spin-LSC approach which only ever requires, at most, N calculations.

These simulations provide useful tests of the numerical performance of various non-adiabatic approaches beyond model systems, which have been used as the main workhorse for benchmarking new methods in the field of quantum dynamics. However, it is our hope that these benchmark studies using realistic, *ab initio* systems will help to foster the development of new quantum dynamics approaches.

II. THEORY

A. The Molecular Hamiltonian

Simulating quantum dynamics of molecular systems amounts to solving the coupled electron-nuclear dynamics governed by the molecular Hamiltonian,

$$\hat{H} = \hat{T}_{\mathbf{R}} + \hat{T}_{\mathbf{r}} + \hat{V}_c(\mathbf{r}, \mathbf{R}) \equiv \hat{T}_{\mathbf{R}} + \hat{H}_{el}(\mathbf{r}, \mathbf{R}), \quad (1)$$

where $\hat{T}_{\mathbf{R}} = -\frac{\hbar^2}{2\mathbf{M}}\nabla_{\mathbf{R}}^2$ and $\hat{T}_{\mathbf{r}} = -\frac{\hbar^2}{2m_e}\nabla_{\mathbf{r}}^2$ is the kinetic energy operator for the nuclear and electronic degrees of freedom (DOF), $\hat{V}_c(\mathbf{r}, \mathbf{R})$ describes the coulomb interactions between all DOF (electronic and nuclear) and $\hat{H}_{el}(\mathbf{r}, \mathbf{R}) = \hat{T}_{\mathbf{r}} + \hat{V}_c(\mathbf{r}, \mathbf{R})$ is the electronic part of the molecular Hamiltonian. Directly simulating quantum dynamics by solving time-dependent Schrödinger equation (TDSE) governed by $\hat{H}$ is intractable. Instead, mixed-quantum classical and semi-classical quantum dynamics approaches offer an efficient but approximate solution to the TDSE. These approaches solve the quantum dynamics in the following two steps.

In the first step, an electronic structure calculation is performed to obtain adiabatic potential energies and gradients. That is, one solves the time-independent Schrödinger equation for the electronic part of the Hamiltonian,

$$\hat{H}_{el}(\mathbf{r}, \mathbf{R})|\epsilon_\mu(\mathbf{R})\rangle = \epsilon_\mu(\mathbf{R})|\epsilon_\mu(\mathbf{R})\rangle, \quad \mathbf{R} \in \{R_a\} \quad (2)$$

where $|\epsilon_\mu(\mathbf{R})\rangle$ and $\epsilon_\mu(\mathbf{R})$ are referred to as the *adiabatic* state and *adiabatic* potential energy surface respectively.

In the second step, one evolves the electronic and nuclear degrees of freedom (DOFs), governed by the total Hamiltonian $\hat{H}$, using the output of the previous step. The total Hamiltonian $\hat{H}$ in the adiabatic representation can be written as,

$$\hat{H} = \sum_a \frac{(\hat{P}_a - i\hbar\hat{d}(R_a))^2}{2M_a} + \sum_\mu \epsilon_\mu(\mathbf{R})|\epsilon_\mu(\mathbf{R})\rangle\langle\epsilon_\nu(\mathbf{R})| \quad (3)$$

where $d_{\mu\nu}(R_a) = \langle\epsilon_\mu(R_a)|\nabla_a|\epsilon_\nu(R_a)\rangle$ is the nonadiabatic coupling vector (NACV), which originates from the nuclear kinetic energy operator $\hat{T}_{\mathbf{R}}$ and appears due to the dependence of the adiabatic states on the nuclear coordinates. The matrix elements (note that diagonal elements are zero, $d_{\mu\mu}(R_a) = 0$) of the NACV can also be expressed as,

$$d_{\mu\nu}(R_a) = \frac{\langle\epsilon_\mu(\mathbf{R})|\nabla_a\hat{H}_{el}|\epsilon_\nu(\mathbf{R})\rangle}{\epsilon_\nu(\mathbf{R}) - \epsilon_\mu(\mathbf{R})}, \quad \mu \neq \nu \quad (4)$$

where the denominator becomes zero at conical intersections or trivial crossings (i.e. $\epsilon_\nu(\mathbf{R}) - \epsilon_\mu(\mathbf{R}) = 0$) making the total Hamiltonian singular. Further, NACV is often very sharp, requiring a small time step to obtain reasonable dynamics. Performing dynamics using $\hat{H}$ given in Eqn. 3 thus becomes numerically challenging.

Barring this numerical challenge, importantly the adiabatic representation also introduces incompatibility challenges for propagating the coupled electronic and nuclear degrees of freedom. This is because many quantum dynamics approaches, such as the spin-mapping approaches used in this work, are instead formulated in the diabatic representation $\{|D_\mu\rangle\}$ are incompatible with the output obtained in the adiabatic representation. Within the diabatic representation $\{|D_\mu\rangle\}$, the NACV vanishes by definition,

$$\langle D_\nu|\nabla_a|D_\mu\rangle = 0, \qquad (5)$$

as the diabatic states $|D_\mu\rangle$ are independent of the nuclear configuration $\{\mathbf{R}\}$. The total molecular Hamiltonian in the diabatic representation has the following preferable compact form,

$$\hat{H}_{\mathrm{D}} = \sum_a \frac{\hat{P}_a^2}{2M_a} + \sum_{\mu\nu} V_{\mu\nu}(\mathbf{R})|D_\mu(\mathbf{R})\rangle\langle D_\nu(\mathbf{R})|, \qquad (6)$$

where $V_{\mu\nu}(\mathbf{R}) = \langle D_\nu(\mathbf{R})|\hat{H}_{\mathrm{el}}(\mathbf{r},\mathbf{R})|D_\mu(\mathbf{R})\rangle$ has off-diagonal matrix elements (called diabatic coupling) in contrast to its adiabatic counter-part $\sum_\mu \epsilon_\mu(\mathbf{R})|\epsilon_\mu(\mathbf{R})\rangle\langle\epsilon_\mu(\mathbf{R})|$ in Eq. 3. In this work, we utilize the quasi-diabatic (QD) framework to directly propagate the quantum dynamics using the outputs obtained in the adiabatic representation. Below, we briefly describe the spin-mapping approach and how it has been interfaced with adiabatic outputs using the QD framework.

B. The Spin-Mapping Approach

In this work, we closely followed the spin-mapping (SM) approach of Richardson and coworkers.[44–47] More specifically, our outline of the theory will closely parallel that of ref. 46 and 47 using the language of Cartesian mapping variables.

Consider the coupled electron-nuclear Hamiltonian with the electronic operators split into state-independent $V_0(\hat{\mathbf{R}})$ and state-dependent $\hat{V}(\hat{\mathbf{R}})$ terms,

$$\hat{H} = \hat{T}_{\hat{\mathbf{R}}} + V_0(\hat{\mathbf{R}}) + \hat{V}(\hat{\mathbf{R}}), \qquad (7)$$

where the trace over the electronic subsystem $Tr_E[\hat{V}(\hat{\mathbf{R}})] = 0$ by construction. Note that $\hat{V}(\hat{\mathbf{R}})$ is an $N \times N$ matrix, where N is the number of considered electronic states.

Many dynamical quantities of interest can be written as a two-time correlation function,

$$C_{AB}(t) = \mathrm{Tr}[\hat{\rho}_b(0)\hat{A}(0)\hat{B}(t)], \qquad (8)$$

where $\hat{A}(0)$ and $\hat{\rho}_b(0)$ can be interpreted as the factorized initial electronic and nuclear configuration for the system at $t = 0$. In this work, we take $\hat{A}$ and $\hat{B}$ to be operators in the $N \times N$ electronic sub-space. $\hat{\rho}_b$ is the nuclear density operator, and the trace is over both nuclear and electronic degrees of freedom (DOFs).

1. Spin-LSC

In the fully linearized spin-mapping framework, any electronic-only, two-operator correlation function can be written as,

$$C_{AB}(t) = \langle A_W(\mathcal{Z}(0)) B_W(\mathcal{Z}(t)) \rangle_{\mathrm{spin-LSC}} \qquad (9)$$

where A_W (B_W) is the Stratonovich-Weyl (SW) transform of the operator $\hat{A}$ ($\hat{B}$),

$$[\hat{A}]_W(\mathcal{Z},0) \equiv A_W(\mathcal{Z}(0)) = Tr[\hat{A}\ \hat{\omega}_W^\dagger(\mathcal{Z}(0))]$$
$$[\hat{B}]_W(\mathcal{Z},t) \equiv B_W(\mathcal{Z}(t)) = Tr[\hat{B}\ \hat{\omega}_W(\mathcal{Z}(t))]. \qquad (10)$$

The SW kernel can be written as,

$$\hat{\omega}_W(\mathcal{Z},t) = \frac{1}{2}\sum_{\mu,\nu}^N \left(\mathcal{Z}_\mu(t)\mathcal{Z}_\nu^*(t) - \gamma_W\delta_{\mu\nu}\right)|\mu\rangle\langle\nu|, \qquad (11)$$

in the electronic basis $\{\mu,\nu\}$ (in the diabatic representation). The kernel is evaluated as a function of the complex-valued, time-evolved mapping variables $\mathcal{Z} = \{\mathcal{Z}_1, \mathcal{Z}_2, ..., \mathcal{Z}_N\}$ with a fixed zero-point energy parameter $\gamma_W = \frac{2}{N}(\sqrt{N+1} - 1)$. One can identify

$$\mathcal{Z}_\mu = q_\mu + ip_\mu \qquad (12)$$

analogously to the commonly used MMST mapping; however, the explicit use of the q and p variables is not required and not used in this work.

The correlation function is evaluated using focused initial conditions such that,

$$\langle\cdots\rangle_{\mathrm{spin-LSC}} \rightarrow \langle\cdots\rangle_{\mathrm{spin-LSC}}^{\mathrm{foc.}}$$
$$\langle\cdots\rangle_{\mathrm{spin-LSC}}^{\mathrm{foc.}} = \sum_\lambda^N \int dRdPd\mathcal{Z}\rho_{\mathrm{b}}(R,P)\cdots\rho_W^{(\lambda)}, \qquad (13)$$

where $\rho_{\mathrm{b}}(R,P)$ is the nuclear Wigner distribution, $\rho_W^{(\lambda)}$ is the initially focused electronic distribution written as,

$$\rho_W^{(\lambda)} = \frac{\delta(|\mathcal{Z}_\lambda|^2 - \gamma_W - 2)\Pi_{\mu\neq\lambda}\delta(|\mathcal{Z}_\mu|^2 - \gamma_W)}{\int d\mathcal{Z}\delta(|\mathcal{Z}_\lambda|^2 - \gamma_W - 2)\Pi_{\mu\neq\lambda}\delta(|\mathcal{Z}_\mu|^2 - \gamma_W)}. \qquad (14)$$

This spin-LSC correlation function using the focused initial sampling (Eq. 13) is evaluated by performing N independent sets of trajectories, one for each λ in the sum in Eq. 13. For each λ, the mapping variables $\mathcal{Z}$ are initialized as,

$$\mathcal{Z}_\lambda = \sqrt{2+\gamma_W}\cdot e^{i\phi_\lambda} \quad \text{(Initially focused state)}$$
$$\mathcal{Z}_\mu = \sqrt{\gamma_W}\cdot e^{i\phi_\mu}, \quad \mu\neq\lambda \qquad (15)$$

with $\{\phi\}$ randomly sampled between 0 and 2π, independently from one another.

In this work, we are only interested in correlation functions with $\hat{A}(0) = |\sigma\rangle\langle\sigma|$, which indicates that the initial electronic density matrix is a single electronic state σ.

This is the case for a time-independent Frank-Condon excitation, often used as the initial condition for non-adiabatic dynamics studies. In this case, the spin-LSC correlation function is greatly simplified to,

$$C_{|\sigma\rangle\langle\sigma|B}(t) = \int dRdPd\mathcal{Z}\rho_{\rm b}(R,P)\rho_W^{(\sigma)}B_W(\mathcal{Z},t), \quad (16)$$

since,

$$A_W = [|\sigma\rangle\langle\sigma|]_W = \delta_{\sigma\lambda}, \quad (17)$$

which picks out a single term in Eq. 13. Since there is no sum over λ in the correlation function, one only needs to converge one set of trajectories ($\lambda = \sigma$ in Eq. 14), which involves sampling the mapping variables as $\mathcal{Z}_\sigma(0) = \sqrt{2+\gamma_W}e^{i\phi_\sigma}$ and $\mathcal{Z}_{\mu\neq\sigma}(0) = \sqrt{\gamma_W}e^{i\phi_\mu}$. Still, one must still ensure that both the random phases $\{\phi\}$ of the mapping variables and the nuclear phase space variables $\{R,P\}$ are sufficiently converged/sampled.

The propagation of the mapping and nuclear variables can be done in the usual MMST manner as,

$$\begin{aligned}
\frac{d\mathcal{Z}_\mu}{dt} &= -i\sum_\nu \langle\mu|\hat{V}(X)|\nu\rangle\mathcal{Z}_\nu, \\
\frac{dR}{dt} &= \frac{P}{M}, \\
\frac{dP}{dt} &= F_0(R) + F_e(R,\mathcal{Z}),
\end{aligned} \quad (18)$$

where $F_0(R)$ are the state-independent forces, and the state-dependent forces $F_e(R,\mathcal{Z})$ are calculated as,

$$F_e(R,\mathcal{Z}) = -\frac{1}{2}\sum_{\mu\nu}\langle\mu|\nabla\hat{V}(R)|\nu\rangle(\mathcal{Z}_\mu(t)\mathcal{Z}_\nu^*(t) - \gamma_W\delta_{\mu\nu}). \quad (19)$$

Finally, the estimator for the reduced density matrix of a single trajectory is simply the population of the mapping variables evaluated at time t, as shown above in the state-dependent force expression,

$$\rho_{\mu\nu}(t) = \frac{1}{2}(\mathcal{Z}_\mu(t)\mathcal{Z}_\nu^*(t) - \gamma_W\delta_{\mu\nu}). \quad (20)$$

2. Spin-PLDM

Following a similar line of reasoning as spin-LSC outlined above, spin-PLDM can be thought of as a natural extension to the fully linearized case of spin-LSC, now incorporating two sets of mapping variables for each electronic state. This extension can be thought of as an extension from a wavefunction representation to a density matrix representation where one set of mapping variables ($\{\mathcal{Z}\}$) represents the "ket" moving forward in time and the other ($\{\mathcal{Z}'\}$) represents the "bra" moving backward in time. In general, the observable quantities can be constructed as an average of these two non-interacting paths in electronic action, only connected through simultaneous interaction with nuclear motion.[46,47,56]

The general correlation function can be written as,

$$\begin{aligned}
C_{AB}(t) &= \\
&\langle\,Tr[\,\hat{A}\hat{\omega}_W^\dagger(\mathcal{Z}',t)\hat{B}\hat{\omega}_W(\mathcal{Z},t)\,]\,\rangle_{\rm spin-PLDM},
\end{aligned} \quad (21)$$

which is in stark contrast to that of Eq. 9 for spin-LSC in that two sets of mapping variables appear ($\{\mathcal{Z}\}, \{\mathcal{Z}'\}$), which now represent the *evolution operator* instead of the operators $\hat{A}$ or $\hat{B}$ explicitly.[46,47] Hence, the spin-LSC and spin-PLDM utilize these SW kernels to represent two vastly different quantities in the correlation function.

Here, the time-evolved SW kernel is slightly modified as,

$$\hat{\omega}(\mathcal{Z},t) = \frac{1}{2}\sum_{\mu,\nu}^N\left(\mathcal{Z}_\mu(t)|\mu\rangle\langle\nu|\mathcal{Z}_\nu^*(0) - \gamma_W\hat{U}(t)\right), \quad (22)$$

where now the time-evolution [acted upon from the left of the kernel as $\hat{\omega}_W(\mathcal{Z},t+\Delta t) = e^{-i\hat{V}(R)\Delta t}\hat{\omega}_W(\mathcal{Z},t)$] now evolves only a single $\mathcal{Z}$ while also evolving the ZPE parameter in time. $\hat{U}(t)$ is evolved at each timestep (Δt) as,

$$\hat{U}(t) = e^{-i\hat{V}(R_N)\Delta t}\cdots e^{-i\hat{V}(R_2)\Delta t}e^{-i\hat{V}(R_1)\Delta t}\mathbb{1}_F, \quad (23)$$

where $\hat{V}(R_n)$ is the state-dependent potential from Eq. 7 evaluated at nuclear configuration R_n after n nuclear timesteps. Note that at $t = 0$, $\hat{U}(0) = \mathbb{1}_N$, which is the identity matrix in the electronic Hilbert space with N states. For spin-LSC, one could say that $\hat{U}(t) = \mathbb{1}_N$ for all time t.

As before, we evaluate the correlation function using focused initial conditions, which can be written as,

$$\begin{aligned}
&\langle\cdots\rangle_{\rm spin-PLDM} \rightarrow \langle\cdots\rangle_{\rm spin-PLDM}^{\rm foc.} \\
&\langle\cdots\rangle_{\rm spin-PLDM}^{\rm foc.} = \\
&\sum_\lambda^N\sum_{\lambda'}^N\int dRdPd\mathcal{Z}\rho_{\rm b}(R,P)\cdots\rho_W^{(\lambda)}\rho_W^{(\lambda')}.
\end{aligned} \quad (24)$$

Note now that the spin-PLDM correlation function has picked up a second sum which focuses the backward mapping variables to electronic state λ'. This additional sampling now impedes the same simplification that was made before for spin-LSC when only computing initial operators $\hat{A} = |\sigma\rangle\langle\sigma|$. Now, in principle, all N^2 focused initial conditions for λ and λ' will play some role in the correlation function at time $t > 0$ no matter the choice of $\hat{A}$.

The mapping variables are initially sampled in the same way as for spin-LSC and completely independently.

$$\begin{aligned}
\mathcal{Z}_\lambda &= \sqrt{2+\gamma_W}\;e^{i\phi_\lambda}; & \mathcal{Z}_\mu &= \sqrt{\gamma_W}\;e^{i\phi_\mu}, & \mu\neq\lambda \\
\mathcal{Z}_{\lambda'}' &= \sqrt{2+\gamma_W}\;e^{i\phi_{\lambda'}'}; & \mathcal{Z}_\mu' &= \sqrt{\gamma_W}\;e^{i\phi_\mu'}, & \mu\neq\lambda',
\end{aligned} \quad (25)$$

where now $\{\phi\}$ and $\{\phi'\}$ are independently and randomly sampled between 0 and 2π. The time-evolution

of the mapping variables is identical to Eq. 18 for the forward and backward DOFs, while the state-dependent nuclear force $F_e(R)$ used to propagate the nuclei $P/M = F_e(R, \mathcal{Z}, \mathcal{Z}')$ is instead computed identically to the standard PLDM prescription as the average over the forward and backward paths,

$$
\begin{aligned}
F_e(R, \mathcal{Z}, \mathcal{Z}') &= \frac{1}{2}\big[F_e(R, \mathcal{Z}) + F_e(R, \mathcal{Z}')\big], \\
F_e(R, \mathcal{Z}) &= \\
&-\frac{1}{2}\sum_{\mu\nu}\langle\mu|\nabla\hat{V}(R)|\nu\rangle\bigg(\mathcal{Z}_\mu(t)\mathcal{Z}_\nu^*(t) - \gamma_W\hat{\mathbb{1}}_N\bigg), \\
F_e(R, \mathcal{Z}') &= \\
&-\frac{1}{2}\sum_{\mu\nu}\langle\mu|\nabla\hat{V}(R)|\nu\rangle\bigg(\mathcal{Z}'_\mu(t)\mathcal{Z}'^*_\nu(t) - \gamma_W\hat{\mathbb{1}}_N\bigg),
\end{aligned}
\tag{26}
$$

Note that here the propagator $\hat{U}(t)$ does not appear, since the representation of an operator ($\nabla\hat{V}(R)$ in this case, see Eq. 10) is written as $[\nabla\hat{V}]_W(\mathcal{Z}) = \mathrm{Tr}\big[\nabla\hat{V}(R)\hat{\omega}(\mathcal{Z})\big]$,

$$
[\nabla\hat{V}]_W(\mathcal{Z}) = \frac{1}{2}\sum_{\mu\nu}\langle\mu|\nabla\hat{V}|\nu\rangle\bigg(\mathcal{Z}_\mu(t)\mathcal{Z}_\nu^*(t) - \gamma_W\delta_{\mu\nu}\bigg),
\tag{27}
$$

for either $\mathcal{Z}$ or $\mathcal{Z}'$ mapping variables just as in spin-LSC, and can be thought of as an average force of the forward and backward paths.

For $\hat{A} = |\sigma\rangle\langle\sigma|$, the estimator for the reduced density matrix at time t of *a single trajectory* can be calculated as,

$$
\begin{aligned}
\rho_{\mu\nu}(t) &= Tr[\,\hat{A}\hat{\omega}_W^\dagger(\mathcal{Z}', t)|\mu\rangle\langle\nu|\hat{\omega}_W(\mathcal{Z}, t)\,] \\
&= \langle\sigma|\hat{\omega}_W^\dagger(\mathcal{Z}', t)|\mu\rangle\langle\nu|\hat{\omega}_W(\mathcal{Z}, t)|\sigma\rangle,
\end{aligned}
\tag{28}
$$

with,

$$
\langle\nu|\hat{\omega}_W(\mathcal{Z}, t)|\sigma\rangle = \frac{1}{2}\big(\mathcal{Z}_\nu(t)\mathcal{Z}_\sigma^*(0) - \gamma_W\delta_{\nu\sigma}\big)
\tag{29}
$$

Recall that the sum of initially focused conditions (λ and λ' from Eq. 24) affects the distribution of the mapping variables ($\mathcal{Z}$, $\mathcal{Z}'$) and so the effect of this focusing does not appear in the estimator explicitly. Additionally, the meaning of a single trajectory in spin-PLDM is rather unclear, since the true correlation function depends not on simple averaging over a statistical ensemble but also over a set of sums $\{\lambda, \lambda'\}$ that, in principle, give different dynamics compared to those focused to a different density matrix element (*i.e.*, an initial state for both the forward and backward components). As such, we will not perform any analysis on individual trajectories from this method.

Finally, we note that if γ_W is set to zero, the standard PLDM formalism[56] is recovered. Instead, if $\mathcal{Z} = \mathcal{Z}'$ and $\hat{U}(t) \to \hat{\mathbb{1}}_N$, then spin-LSC is recovered.

C. Quasi-diabatic Propagation

Here, we briefly outline the QD scheme used in this work to connect the spin-mapping approaches, originally formulated in the diabatic quantum representation, with the adiabatic electronic structure calculations. For more details on the QD scheme in general, we refer the reader to Refs. 57,62,70,71.

Upon performing the electronic structure calculation at the initial nuclear configuration $\mathbf{R}(0)$ to obtain the necessary adiabatic quantities: diagonal energies $\epsilon_\mu(0)$ and nuclear gradients $\nabla_\mathbf{R}V_{\mu\nu}(0) = \langle\epsilon_\mu(0)|\nabla_\mathbf{R}\hat{H}_{el}|\epsilon_\nu(0)\rangle = \mathbf{d}_{\mu\nu}*(\epsilon_\nu(0)-\epsilon_\mu(0))$, where $\mathbf{d}_{\mu\nu} = \langle\epsilon_\mu(0)|\nabla_\mathbf{R}|\epsilon_\nu(0)\rangle/(\epsilon_\nu - \epsilon_\mu)$ (see Eq. 4). After calculating the initial force $\mathbf{F}(0)$ in the mapping representation (Eq. 19) and propagating the nuclear DOFs via a velocity-Verlet scheme, a second electronic structure calculation is performed at the updated nuclear coordinated $\mathbf{R}(\Delta t)$ to obtain the necessary adiabatic quantities: diagonal energies $\epsilon_\mu(\Delta t)$, nuclear gradients $\nabla_\mathbf{R}V_{\mu\nu}(\Delta t) = \langle\epsilon_\mu(\Delta t)|\nabla_\mathbf{R}\hat{H}_{el}|\epsilon_\nu(\Delta t)\rangle = \mathbf{d}_{\mu\nu}*(\epsilon_\nu(\Delta t) - \epsilon_\mu(\Delta t))$, and the time-overlap matrix $S_{\mu\nu}(0, \Delta t) = \langle\epsilon_\mu(0)|\epsilon_\nu(\Delta t)\rangle$.

Next, the electronic mapping variables are propagated using an linearly interpolated Hamiltonian between the time 0 and Δt in the basis of adiabatic electronic states at time 0. The unitary rotation between the time Δt and time 0 bases is exactly the time-overlap matrix $S(0, \Delta t)$. Explicitly, the diagonal energies at time Δt, $[\epsilon(\Delta t)]$, are rotated to the time 0 basis as $H(\Delta t) = S(0, \Delta t) \times [\epsilon(\Delta t)] \times S^\mathrm{T}(0, \Delta t)$, which forms an off-diagonal Hamiltonian matrix. Here $[\epsilon(\Delta t)]$ implies a matrix representation of the diagonal adiabatic energies $\epsilon_\mu(\Delta t)$. The linearly interpolated Hamiltonian then takes the form $H(t) = [\epsilon(0)] + \frac{t-0}{\Delta t}\big(H(\Delta t) - [\epsilon(0)]\big)$, where $t \in (0, \Delta t)$. The mapping variables are propagated using a velocity-Verlet scheme (by splitting the real and complex components of $\mathcal{Z}$) which solves the first equation in Eq. 18 for spin-LSC for spin-PLDM, noting the only difference is that the spin-PLDM contains two sets of mapping variables $\{\mathcal{Z}, \mathcal{Z}'\}$ that are propagated independently from one another. Finally, the mapping variables are rotated to the time Δt basis via the time-overlap matrix $S(0, \Delta t)$ as $S^\mathrm{T}(0, \Delta t) \times \mathcal{Z}(\Delta t) \to \mathcal{Z}(\Delta t)$.

Furthermore, in spin-PLDM, the ZPE matrix $U(0) = \mathbb{1}$ (identity matrix at time 0) needs to be propagated according to $U(\Delta t) = \exp[-i\hat{H}\Delta t]U(0)$, which is done in the time Δt basis after the ZPE matrix has been rotated to the Δt basis such that the Hamiltonian is diagonal $[\epsilon(\Delta t)]$ and only applies a phase shift in addition to the time-overlap transformation. The entire ZPE matrix basis rotation and subsequent time-propagation can be compactly written as $U(\Delta t) = e^{-i\hat{H}\Delta t} \times S^\mathrm{T}(0, \Delta t) \times U(0) \times S(0, \Delta t) = e^{-i[\epsilon(\Delta t)]\Delta t} \times S^\mathrm{T}(0, \Delta t) \times U(0) \times S(0, \Delta t)$.

The above procedure is repeated for the desired number of nuclear time-steps, replacing all time 0 quantities with time Δt quantities (*i.e.*, the new reference basis)

and further propagating the nuclei to acquire the time $2\Delta t$ adiabatic quantities.

D. Computational Details for Ab Initio Simulations

The non-adiabatic molecular dynamics simulations use an in-house-modified version[71] of the SHARC non-adiabatic molecular dynamics code,[72] interfaced to the MOLPRO electronic structure package.[73] On-the-fly electronic structure calculations are performed at the level of state-averaged complete active space self-consistent field (SA-CASSCF) approach. Ethylene, fulvene, methyliminium cation, and 1,2-dithiane were calculated with 3SA-CASSCF(2,2), 2SA-CASSCF(6,6), 2SA-CASSCF(6,5), and 3SA-CASSCF(6,4), respectively. All simulations were performed with the 6-31G* basis set. These SA-CASSCF parameters were taken from Refs. 67 and 68. In all cases, only the two lowest-energy, singlet adiabatic states, S_0 and S_1, were used in the electronic dynamics with the initial electronic state always set to the first singlet excited state, S_1. Unless otherwise specified, in all *ab initio* results, the timestep for the nuclear propagation was 0.1 fs using 200 electronic substeps per nuclear step. Further, 1000 trajectories were computed for each molecular model. To be clear, in the spin-PLDM correlation function, each initially focused electronic conditions $\{\lambda, \lambda'\}$ was converged with the 1000 trajectories, in total $2 \times 2 \times 1000 = 4000$ trajectories for each of the two-state chemical models.

The initial Wigner distribution is sampled from the ground vibrational state $\nu = 0$ on the ground electronic state $|S_0\rangle$, where the normal mode frequencies (in the harmonic approximation) are calculated based on the approach outlined in Refs. 74 and 75, as implemented in the SHARC package.[72] For all molecules, the normal mode frequencies are computed at the level of MP2/6-31++G** with the MOLPRO package, with the optimized structure obtained at the same level of electronic structure theory for the ground electronic state. In particular, the nuclear density $\rho_W(\tilde{\mathbf{R}}, \tilde{\mathbf{P}})$ in terms of the molecular normal-mode frequencies $\{\tilde{\omega}_k\}$ and phase space variables $\{\tilde{\mathbf{R}}, \tilde{\mathbf{P}}\}$ is given as[76]

$$\rho_{\mathrm{W}}(\tilde{\mathbf{R}}, \tilde{\mathbf{P}}) \propto \prod_{k=1}^{\mathcal{N}} \exp[-\tanh(\frac{\beta\hbar\tilde{\omega}_k}{2})(\frac{m\tilde{\omega}_k}{\hbar}\tilde{R}_k^2 + \frac{1}{m_k\tilde{\omega}_k\hbar}\tilde{P}_k^2)]. \tag{30}$$

The initial distribution $\{\mathbf{R}, \mathbf{P}\}$ is then obtained by transforming $\{\tilde{\mathbf{R}}, \tilde{\mathbf{P}}\}$ from the normal mode representation to the primitive coordinates using the unitary transformation that diagonalizes the Hessian matrix. The positions and momenta for all molecules except for fulvene were sampled from the above Wigner distribution. For fulvene, only the coordinates were sampled and the momenta were set to zero, such that the molecule encounters only the slanted conical intersection.[67]
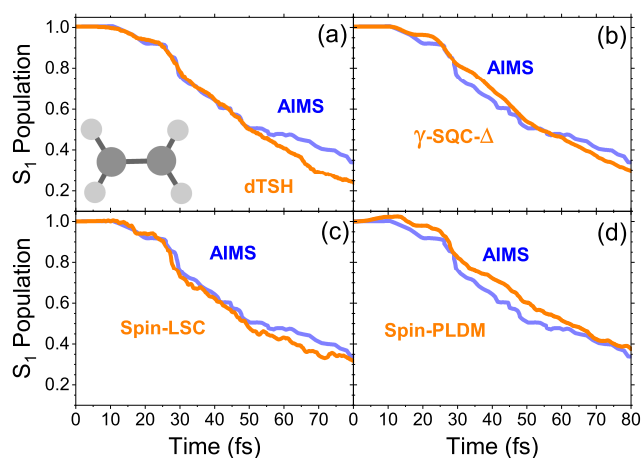

FIG. 1. S_1 population dynamics of the ethylene molecule at the SA(3)-CASSCF(2,2)/6-31G* level of theory for a variety of semi-classical methods: (a) dTSH, (b) γ-SQC-Δ, (c) spin-LSC, and (d) spin-PLDM. All methods are compared to the *ab initio* multiple spawning (AIMS) result, which is taken to be more exact compared to these semi-classical approaches. The AIMS and dTSH results were taken from Ref. 67.

III. RESULTS AND DISCUSSION

Fig. 1 presents the photodissociation of ethylene through its S_1/S_0 conical intersection generated by the rotation of the H-C-C-H dihedral angle. The nuclear dynamics of ethylene are analogous to the dynamics of the molecular Tully model #1,[77] as discussed in previous reports.[54,62,67] In this model and *ab initio* system, the wavepacket encounters a single nonadiabatic event, a conical intersection (CI) in this case. This localized crossing represents the simplest nonadiabatic effect in the present work, which is demonstrated by the simplistic population dynamics in Fig. 1. Even so, all of the semiclassical quantum dynamics approaches fail to capture the entirety of the population dynamics compared to the AIMS benchmark (blue).

Fig. 1a shows the popular decoherence-corrected surface hopping approach (dTSH)[78], which is a popular method that captures much of the decoherence that standard FSSH fails to capture. Fig. 1b presents the γ-corrected SQC approach using the triangle windowing (γ-SQC-Δ). Fig. 1c and Fig. 1d show the two new approaches of this work: spin-LSC and spin-PLDM, respectively. At short times (less than 30 fs), all methods capture the correct population dynamics which exhibits 10 fs of plateau followed by a short decrease and another short plateau (*i.e.*, a shoulder). Though, dTSH and spin-LSC capture the AIMS result better than γ-SQC-Δ and spin-PLDM. At medium times (more than 30 fs and less than 50 fs), only dTSH is able to capture the AIMS result, followed closely by spin-LSC. Both γ-SQC-Δ and spin-PLDM overestimate the population in the S_1 state. At longer times, none of the methods accurately capture the AIMS result; however, spin-LSC captures the over-
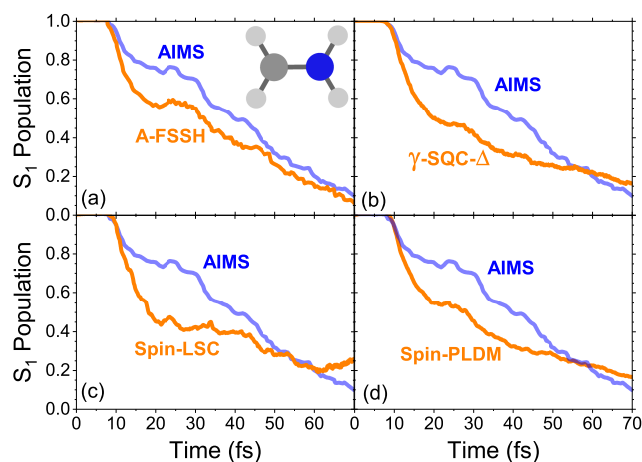
FIG. 2. S_1 population dynamics of the $CH_2NH_2^+$ molecule at the SA(2)-CASSCF(6,5)/6-31G* level of theory for a variety of semi-classical methods: (a) A-FFSH, (b) γ-SQC-Δ, (c) spin-LSC, and (d) spin-PLDM. All methods are compared to the *ab initio* multiple spawning (AIMS) results, which are taken to be more exact compared to these semi-classical approaches. The AIMS and A-FFSH results were taken from Ref. 68.

all trends the best at all times, though underestimating the S_1 population at longer times. For the molecular systems simulated here, Spin-PLDM seems to overestimate the population at all times. Furthermore, the initial S_1 population (between 0 and 15 fs) goes above 1.0, which implies that 1000 trajectories were not sufficient to fully converge this correlation function. Recall, the cost of spin-PLDM scales poorly with the number of states N, since N^2 converged population dynamics: 1000×2^2 trajectories in this case, $4\times$ more expensive than spin-LSC, γ-SQC-Δ, and dTSH. However, as we will discuss later (in Fig. 7), a major simplification of spin-PLDM can be made by excluding some of the N^2 initial conditions present in the full spin-PLDM correlation function. Overall, all four approaches capture the general physics of ethylene CI dynamics. Thus, a strict delineation of each method's quality is not straightforward.

Fig. 2 provides a slightly more challenging system: the methyliminium cation ($CH_2NH_2^+$). This model is very similar to ethylene in the sense that a CI is generated by the changing H-C-N-H dihedral angle. As such, the benchmark AIMS results suggest that the population dynamics have very similar features as the ethylene dynamics; however, a recurrence/shoulder in the population of the S_1 state appears around 25-30 fs. For this system, all methods, including augmented FSSH (A-FSSH)[79] and the mapping approaches, overestimate the initial population transfer to the ground state around 10 fs. Following this, all approaches seem to provide a plateau in the population of the S_1 state, but only A-FSSH, γ-SQC-Δ, and spin-PLDM are able to showcase a visible recurrence in the S_1 population. Throughout the entire dynamics, A-FSSH seems to capture all of the features found in the
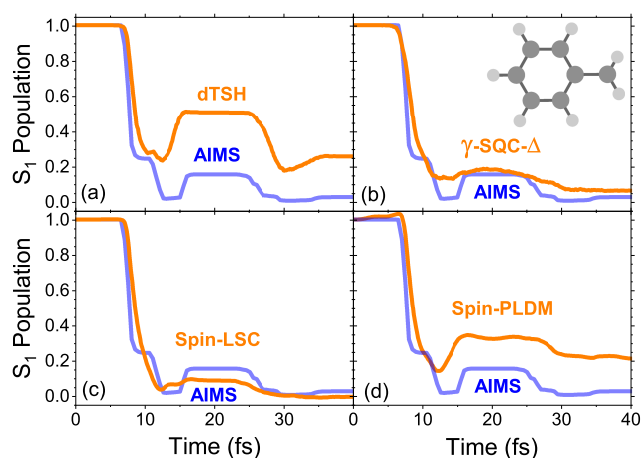

FIG. 3. S_1 population dynamics of the fulvene molecule at the SA(2)-CASSCF(6,6)/6-31G* level of theory for a variety of semi-classical methods: (a) dTSH, (b) γ-SQC-Δ, (c) spin-LSC, and (d) spin-PLDM. All methods are compared to the *ab initio* multiple spawning (AIMS) result, which is taken to be more exact compared to these semi-classical approaches. The AIMS and dTSH results were taken from ref. 67.

AIMS result, with spin-PLDM and γ-SQC-Δ close behind, but both of which overestimate the S_1 population (or rather underestimate the population transfer rate to the ground state) at long times (more than 50 fs). For this model, it is clear that spin-LSC performs worse than the other models while A-FSSH performs well compared to the AIMS result.

Fig. 3 represents a more complicated nonadiabatic scenario in which the fulvene molecule undergoes a periodic (every $\sim 10 - 20$ fs) and extended encounter with an S_0/S_1 CI directly linked to the stretching of the C-CH$_3$ stretching mode. This is similar to the Tully model #3[54,62,67,77] which exhibits a region of strong and extended coupling followed by branching and recrossing of the reflected wavepacket. In this case, the dTSH approach (Fig. 3a) fails to capture the AIMS dynamics at any point in the nonadiabatic dynamics, overestimating the AIMS results by more than 25%. However, dTSH does capture the qualitative trends in the population dynamics. Fig. 3b and Fig. 3c show the γ-SQC-Δ and spin-LSC approaches, respectively, both of which closely follow the AIMS result but neither are able to capture the fine structure of the population near 10 fs nor at 28 fs. dTSH, however, is able to find the fine structure at 10 fs, even though the overall resulting population is not correct after the event. This points to the fact that the dTSH result includes the forces stemming from a single adiabatic surface at a time and not its mean-field surface as is the case for both spin-LSC and γ-SQC-Δ. Finally, the spin-PLDM result shows population dynamics very similar to dTSH and overestimates the population of the excited state at almost all times. Further, spin-PLDM is not able to capture the fine structure of the population at 10 fs. However, like all the methods presented, spin-PLDM does capture the general physics of the fulvene nonadiabatic dynamics.

To further probe the dynamics of fulvene, we examine the averaged nuclear density of a single DOF and subsequent single trajectory properties of the spin-LSC approach. Recall
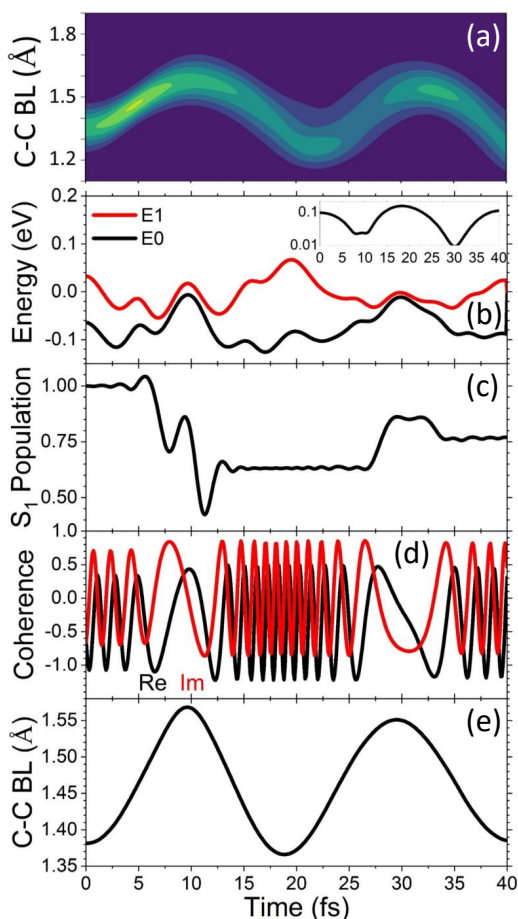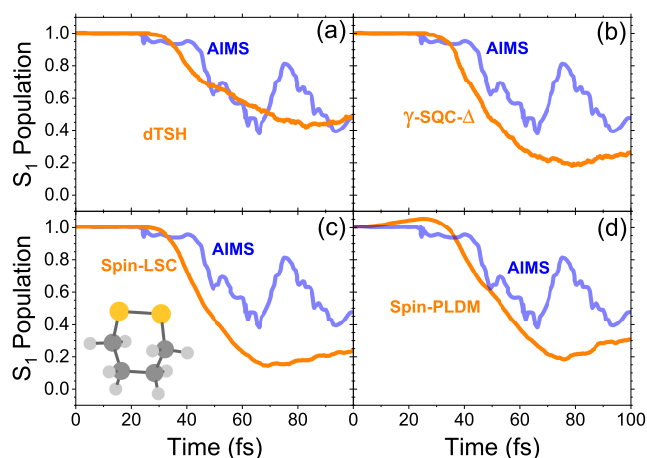
FIG. 5. S_1 population dynamics of the 1,2-dithiane molecule at the SA(3)-CASSCF(2,2)/6-31G* level of theory for a variety of semi-classical methods: (a) dTSH, (b) γ-SQC-Δ, (c) spin-LSC, and (d) spin-PLDM. All methods are compared to the *ab initio* multiple spawning (AIMS) results, which is taken to be more exact compared to these semi-classical approaches. The AIMS result was taken from Ref. 69. Note that a limited number of initial nuclear geometry/momentum samples (*i.e.* 14) were used in the AIMS simulation. We refer the reader to **Appendix A** and Fig. 8 for discussions regarding this issue.

FIG. 4. (a) Fulvene C-C (ring carbon - methyl carbon) bond length density/wavepacket, composed using the same spin-LSC trajectories as provided in the construction of Fig. 3c. (b-e) Observables of a single representative trajectory, including time-dependent (b) energies of the S_0 (black) and S_1 (red) electronic adiabatic states, (c) population of initially populated S_1 state, (d) real (black) and imaginary (red) S_0/S_1 electronic coherence, and (e) C-C bond length. The inset in panel b shows the energy difference between S_1 and S_0 on a log scale.

that a single trajectory in spin-PLDM is less representative than a single trajectory in any other approach since the correlation function depends on a sum of vastly different initial conditions (see Eq. 24) for the mapping variables and thus subsequent nuclear dynamics. Therefore, we omit any further study of spin-PLDM beyond the population dynamics and the averaged contributions to the correlation function itself (to be discussed later in Fig. 7).

Fig. 4a shows the probability density for the C-C bond stretching coordinate of the 1000-trajectory spin-LSC simulation of the fulvene molecule. The wavepacket oscillates, generating the CI at each maximal value of stretching. At long times, the wavepacket broadens slightly but not by an appreciable amount since the C-C bond is never broken. During the simulation, only two oscillations of this bond are allowed. Fig. 4b-e show a single trajectory of the fulvene dynamics, showing (Fig. 4b) the energies of the S_1 (red) and S_0 (black) adiabatic states, (Fig. 4c) the population of the S_1 state,

(Fig. 4d) the real (black) and imaginary (red) parts of the coherence, and (Fig. 4e) the single-trajectory C-C bond stretching coordinate. The potential energy landscape through time is indicative of the prolonged nonadiabatic region analogous to the Tully model #3 and correlates with the extended C-C bond length occurring at 10 and 30 fs. The inset in Fig. 4b shows the energy difference of the S_1 and S_0 states on a log scale.

The population dynamics for this trajectory showcase the complicated nonadiabatic event at 10 fs which all mapping approaches fail to capture once averaged over the 1000 trajectories. While the single trajectory population does not match the AIMS result in magnitude of population, it shows the fine structure (a short plateau/recurrence in S_1 population) of the AIMS result at 10 fs which becomes absent upon trajectory-average. Furthermore, the dynamical evolution of S_1/S_0 coherence is readily available from the spin-LSC approach, and correctly indicates regions of the strong coupling by the dynamic oscillation frequency primarily dictated by the inverse of the energy difference of the electronic states.

As our final molecular example, we present the population dynamics of the 1,2-dithiane molecule upon excitation to the S_1 state. This model showcases an extended CI between S_1 and S_0 which manifests as the S-S bond breaks. Periodically, roughly every 300 fs, the S-S bond reforms and thus moves the system away from the CI. Fig. 5 shows the population dynamics, which for the benchmark AIMS result showcases non-trivial S_1 population recurrences while the system is in the CI. During this time (starting from $\sim$ 30 fs), the energies of the S_1 and S_0 state are degenerate for 100's of fs (see Fig. 6b). In contrast to the AIMS result, all other approaches provide
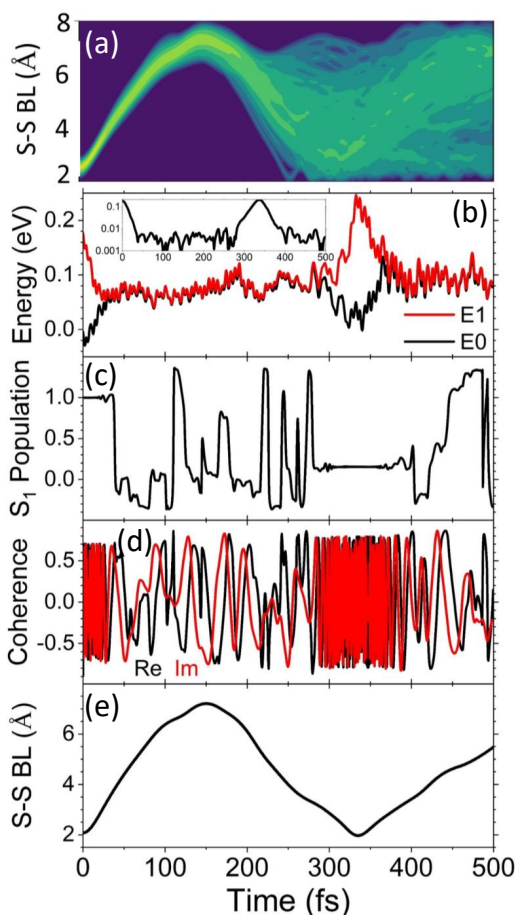
FIG. 6. (a) 1,2-dithiane S-S bond length density/wavepacket, complementary to the data in Fig. 5c. (b-e) Observables of a single representative trajectory, including time-dependent (b) energies of the S_0 (black) and S_1 (red) electronic adiabatic states, (c) population of initially populated S_1 state, (d) real (black) and imaginary (red) S_0/S_1 electronic coherence, and (e) S-S bond length. The inset on panel b shows energy difference between S_1 and S_0 on a log scale. It is important to note that only 200 trajectories were used in the construction of panel a and with a larger time step of $dt = 0.5$ fs due to the computational cost of the extended time scale of 500 fs compared to 100 fs shown in Fig. 5.

smooth population dynamics. AIMS predicts a slight population transfer starting at 25 fs followed by a plateau until 40 fs. All other methods provide 30 fs of negligible population transfer from S_1 to S_0 with no subsequent plateau. The dTSH approach (Fig. 5a) shows the closest correspondence with the AIMS result while the other approaches overestimate the population transfer to the ground state. Overall, none of the other approaches provide the fine structure of the AIMS result, but all approaches provide the correct physics of the molecular dynamics with dTSH performing the best. Note that a limited number of initial nuclear geometry/momentum samples (*i.e.* 14) were used in the AIMS simulation. We refer the reader to **Appendix A** and Fig. 8 for discussions regarding this issue.

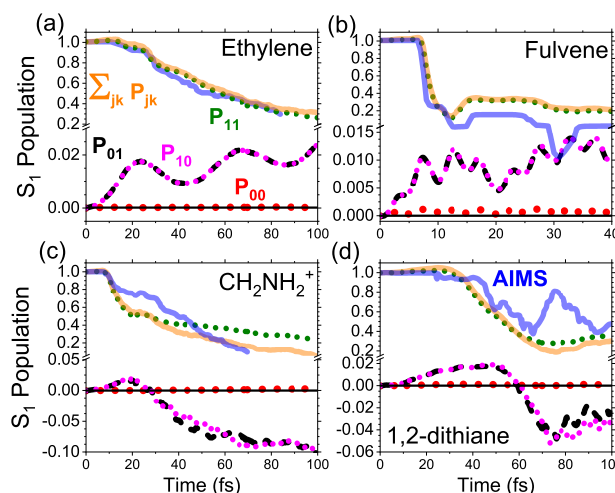In a similar fashion as for the fulvene molecule, in Fig. 6

FIG. 7. S_1 population dynamics for all atomistic models, (a) ethylene, (b) fulvene, (c) $CH_2NH_2^+$, and (d) 1,2-dithiane, using the spin-PLDM method. The thick, solid lines are the same data for AIMS (blue) and spin-PLDM (orange) in previous figures for comparison. The dotted curves showcase the the partial components $P_{\lambda\lambda'}$ of the spin-PLDM correlation function for the population (a single $\lambda\lambda'$ term in the sum in Eq. 24), which decomposes each of the $N^2 = 4$ initially focused conditions of the electronic density matrix.

we present a closer look at the nuclear dynamics of 1,2-dithiane for the spin-LSC approach as well as quantities from a single-trajectory. Fig. 6a shows the density of the S-S bond length across 200 trajectories at an extended time scale of 500 fs. Note that Fig. 5 only showed results up to 100 fs due to the limited AIMS data and with 1000 trajectories. In contrast to the C-C bond length density shown in Fig. 4a, the S-S bond breaks and allows the nuclear wavepacket to broaden due to the larger conformational space. The potential energies of a single trajectory are shown in Fig. 6b and clearly showcase the extended degeneracy of the ground and first excited states, starting from ~30 fs until ~300 fs when the S-S bond is reforming (see single-trajectory S-S bond length in Fig. 6e). The population of the excited state is shown in Fig. 6c along with the coherences in Fig. 6d. The population varies rapidly between the ground and excited state during the regions of degeneracy (30-300 fs) and implies that, unlike the fulvene molecule, trajectory averaging is required for the 1,2-dithiane system in order to make any prediction regarding the populations due to the immense and prolonged coupling between the states. Similarly, the coherence showcases equally complicated behavior in the regions of degeneracy.

While the results of the spin-PLDM approach in these ab initio test cases did not provide superior accuracy compared to SH, SQC, or spin-LSC methods, it is worthwhile to take a closer look at the spin-PLDM correlation function to better understand the approach, especially given that PLDM approach usually provides more accurate dynamics in system-bath models. Fig. 7 presents

the partial contributions $P_{\lambda\lambda'}$ to the total spin-PLDM correlation function $C_{AB} = \sum_{\lambda\lambda'} P_{\lambda\lambda'}$ (Eq. 24) for all four molecular models explored in this work. The total spin-PLDM correlation function requires a summation of overall possible initially focused conditions $\{\lambda, \lambda'\}$ of the electronic mapping variables $\{\mathcal{Z}, \mathcal{Z}'\}$, leading to N^2 initial conditions that need to be converged with respect to the number of trajectories ($1000 \times F^2 = 4000$ trajectories in this work).

Fig. 7a shows the population of the excited state for the AIMS result (blue) as well as the total spin-PLDM correlation function (orange). The dotted lines represent the partial contributions to the spin-PLDM correlation function. The green dotted line is the case where $\lambda\lambda' = 11$ and hence has an initial value of 1.00 since this was the intended initial photo-excitation of the system. This condition appears only in the definition of the operator $\hat{A} = |1\rangle\langle 1|$, which is in principle not implemented until after all N^2 simulations are completed in the post-processing by explicitly performing the trace $\text{Tr}[\hat{A}\hat{\omega}^\dagger(\mathcal{Z}', t)\hat{B}\hat{\omega}(\mathcal{Z}, t)]$ once the time-dependent kernels are known for each $\lambda\lambda'$ condition. The other components cannot start with any other value than 0.0 at the initial time but can accumulate population at later times, as pointed out in Ref. 46,47. In this model, only the off-diagonal initial conditions $\lambda\lambda' = 01, 10$ appreciably contribute to the total population. At the final time, together they contribute up to 5.0% of the total population.

For fulvene in Fig. 7b, a similar trend emerges where the off-diagonal initial conditions generate the most population contribution while the diagonal initial condition (*i.e.*, P_{00}) does not. These trends apply to the final two molecular models as well. However, the off-diagonal contributions in the latter two molecules, $[CH_2NH_2]^+$ and 1,2-dithiane, at long times, are negative, thereby diminishing the population generated by the P_{11} contribution. In fact, the off-diagonal contributions present in the $[CH_2NH_2]^+$ and 1,2-dithiane dynamics represent up to 20% and 10% at a long time. Furthermore, the ethylene and fulvene molecules exhibit periodic-like contributions from the off-diagonal initial conditions while the other two showcase non-periodic population dynamics. It was expected that the ethylene and $[CH_2NH_2]^+$ partial contributions would look similar to one another due to the similarity of the non-adiabatic event present in each molecule, but this was not observed.

For systems with many electronic states, the number of trajectories required to converge all the partial contributions can become unmanageable. Thus one needs to resort to some approximation for the simulations. It is our experience that the spin-PLDM correlation function can be adequately represented by two approximations to the total correlation function by ignoring some of the partial contributions. The first approximation is to simply ignore all contributions except the initially excited state. In each of our models in this work, that amounts to keeping only the P_{11} contribution. In the *ab initio* models explored in this work, the P_{11} population represents at

least 88% of the total contribution, at worst. The next best approximation is to take only the single diagonal contribution which corresponds to the initial excitation, P_{ii} where i is the initial excited state as well as a single column (or row) of the density matrix that includes this initial excitation, $P_{i\lambda}$, for example, with twice the weight. In other words, the approximation amounts to $P_{\text{Total}} = P_{ii} + \sum_\lambda 2P_{i\lambda}$, where the factor 2 accounts for the equal contribution from both the $P_{i\lambda}$ and $P_{\lambda i}$ terms (as shown in Fig. 7 since $P_{01} \approx P_{10}$). This approximation amounts to only N converged initial conditions instead of N^2 as prescribed by the total correlation function.

Neglecting the other diagonal initial conditions is corroborated by the results of the main text, where the P_{00} never contributed any appreciable amount of population. The other off-diagonal initial conditions $P_{\lambda\lambda'}$ where $\lambda \neq i$ and $\lambda' \neq 1$ require an examination of a system with more than two electronic states. Fig. S1 in the **Supporting Information** presents the population dynamics for the FMO 7-state model system[46,47] which has been previously studied with spin-PLDM and achieves superior accuracy compared to FSSH, SQC, and spin-LSC, matching the benchmark hierarchical equations of motion (HEOM) result. Fig. S2a presents the partial contributions to the ground state S_0 population as well as the single-column approximation which yields the same accuracy as the full spin-PLDM correlation function result with 7 converged simulations instead of 49, *a reduction of 86% in computational cost*. The other diagonal and off-diagonal initial conditions are shown in Figs. S2b,c and show less than 0.3% contribution at all times.

IV. CONCLUSIONS

In this work, we use the quasi-diabatic propagation scheme to directly interface the diabatic linearized (spin-LSC) and partially linearized (spin-PLDM) spin-mapping approaches[44–47] and the CASSCF on-the-fly electronic structure calculations to propagate *ab initio* non-adiabatic dynamics. We have performed on-the-fly simulations for four recently suggested molecules, ethylene, fulvene, methyliminium cation ($CH_2NH_2^+$), and 1,2-dithiane.[67–69] These molecular models provide examples of common non-adiabatic phenomena found ubiquitously in realistic systems, namely conical interactions and avoided crossings and are closely related to the well-known simple curve crossing models of Tully.[77]

We have shown that the spin-LSC method provides very accurate non-adiabatic population dynamics when comparing to *ab initio* multiple spawning (AIMS),[67–69] exhibiting a similar level of accuracy to the recently developed symmetric quasi-classical (SQC) approach of Miller and coworkers with a trajectory-adjusted zero-point energy parameter[43] and that of trajectory surface hopping (TSH) with energy-based decoherence corrections.[67] See our previous report on SQC dynamics in Ref. 62 using similar molecular models. However, the

more involved spin-PLDM dynamics exhibit an equivalent or decrease in accuracy in the population dynamics for all models studied, with the Fulvene model (Fig. 3) showcasing the least accurate results.

We further explored the nature of the spin-PLDM correlation function by examining the various components (initially focused contributions λ and λ') individually. Here we noted that when calculating an initial population element $|\sigma\rangle\langle\sigma|$, the off-diagonal initially focused conditions $\sigma\lambda$ (where $\lambda \neq \sigma$) contribute nearly the same magnitude and sign to the overall correlation function as $\lambda\sigma$. Thus, calculating one and doubling its weight provides the same contribution to the total correlation function. Further, the other diagonal contributions $\lambda\lambda$ (with $\lambda \neq \sigma$) have minimal magnitude in their contribution to the overall correlation function and can be ignored. In this sense, an approximate scheme can be constructed, at least in these few example systems explored in this work. In this case, one only needs to calculate a single column of initially focused density matrix elements, $\sigma\lambda$, which reduces the computational cost from N^2 to N converged simulations, still amounting to more computations than the spin-LSC approach which only ever requires one converged initial condition given an initial excitation to $|\sigma\rangle\langle\sigma|$.

These calculations provide useful and non-trivial tests to systematically investigate the numerical performance of various recently developed diabatic quantum dynamics approaches, going beyond the simple diabatic model systems that have historically been the major workhorse in the quantum dynamics field. At the same time, we hope these available benchmark studies will also foster the development of new quantum dynamics approaches.

AVAILABILITY OF DATA

The data that support the findings of this study are available from the corresponding author upon a reasonable request.
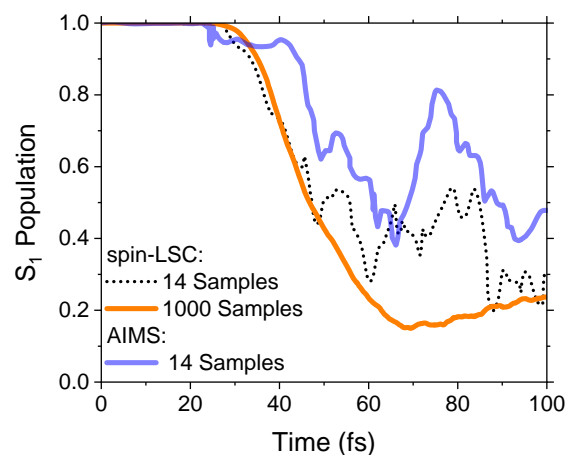

FIG. 8. S_1 population dynamics of the 1,2-dithiane molecular model for the spin-LSC (orange and dotted curves) and AIMS (blue curve) approaches. To directly compare the spin-LSC method to the benchmark AIMS result (data taken from Ref. 69), the spin-LSC was performed using the same 14 initial geometry/momenta as used in and provided by Ref. 69. The 1000-sample spin-LSC (orange) and the 14-sample AIMS (blue) are identical to the data provided in Fig. 5c.

Appendix A: Initial Conditions and Convergence of Population Dynamics

The comparison between the mean-field approaches and AIMS for the 1,2-dithiane molecular species (Fig. 5) was significantly worse than the other molecular models. While this discrepancy can be at least partially attributed to the quality of the MQC approaches and the complexity of the 1,2-dithiane dynamics of an extended region of degeneracy between the ground and excited state, we briefly examine the quality and robustness of the initial conditions of the original AIMS data provided in Ref. 69.

In the original work,[69] the authors used 14 unique initial geometries and momentum sampled from the Wigner distribution for their AIMS calculations. Furthermore, the authors used these 14 nuclear samples 8 times with different random seeds, for a total of 112 trajectories. A major limitation of these results is the limited amount of the geometry/momenta sampled at the beginning. These limited numbers of nuclear samples were chosen due to the large computational cost of the AIMS dynamics simulations. However, to understand the large discrepancies between the AIMS results and MQC populations, we explore the dependence of the spin-LSC results on the reduced initial nuclear sampling identical to the AIMS result.

Using the same 14 nuclear geometries and momenta provided in the Supporting Information of Ref. 69, we performed spin-LSC dynamics on the 1,2-dithiane molecular system to compare to the fully converged spin-LSC (using 1000 nuclear samples). Fig. 8 shows the S_1 popu-

lation dynamics for the AIMS approach with 14 nuclear samples (solid blue curve) and the spin-LSC approach with 1000 nuclear samples (solid orange curve). Both of these results are duplicated from Fig. 5c. The dotted black curve shows the spin-LSC result using the same 14 initial geometries and momenta as the AIMS result. A vast majority of the features in the population dynamics of AIMS are recovered and can be directly attributed to a lack of convergence in the nuclear sampling scheme. Since similar numbers of nuclear samplings were performed for the other three molecular models, the AIMS results are to be taken as a qualitative result for the population dynamics.

While the AIMS approach is in principle a rigorous path toward the exact dynamics of photo-excited molecular systems, the computational cost of this approach sometimes forces the user to relax the parameters necessary for convergence, especially for the number of initial Gaussian functions. We suggest caution when using such results for a benchmark against more approximate methods such as novel MQC approaches. Thus, care must be taken when comparing the MQC results to these high-level benchmarks, keeping in mind that the convergence of the parameters/initial conditions for these wavepacket approaches is paramount to the quality of the results.

[1] J. C. Tully, J. Chem. Phys. **93**, 1061 (1990).
[2] J. Q. M. Ben-Nun and T. J. Martinez, J. Phys. Chem. A **104**, 5161 (2000).
[3] D. A. Micha, J. Phys. Chem. A **103**, 7562 (1999).
[4] S. Bonella and D. F. Coker, J. Chem. Phys. **114**, 7778 (2001).
[5] G. A. Worth, M. A. Robba, and I. Burghardt, Faraday Discuss. **127**, 307 (2004).
[6] N. Ananth, C. Venkataraman, and W. H. Miller, J. Chem. Phys. **127**, 084114 (2007).
[7] P. Huo and D. F. Coker, J. Chem. Phys. **135**, 201101 (2011).
[8] F. Plasser, G. Granucci, J. Pittner, M. Barbatti, M. Persico, and H. Lischka, J. Chem. Phys. **137**, 22A514 (2012).
[9] K. Saita and D. V. Shalashilin, J. Chem. Phys. **137**, 22A506 (2012).
[10] D. V. Makhov, W. J. Glover, T. J. Martinez, and D. V. Shalashilin, J. Chem. Phys. **141**, 054110 (2014).
[11] S. J. Cotton and W. H. Miller, J. Chem. Phys. **139**, 234112 (2013).
[12] S. J. Cotton and W. H. Miller, J. Phys. Chem. A **117**, 7190 (2013).
[13] N. Ananth, J. Chem. Phys. **139**, 124102 (2013).
[14] C.-Y. Hsieh and R. Kapral, J. Chem. Phys. **138**, 134110 (2013).
[15] J. O. Richardson and M. Thoss, J. Chem. Phys. **139**, 031102 (2013).
[16] A. R. Menzeleev, F. Bell, and T. F. Miller, J. Chem. Phys. **140**, 064103 (2014).
[17] G. A. Meek and B. G. Levine, J. Phys. Chem. Lett. **5**, 2351 (2014).
[18] J. E. Subotnik, A. Jain, B. Landry, A. Petit, W. Ouyang, and N. Bellonzi, Annu. Rev. Phys. Chem. **67**, 387 (2016).
[19] T. Nelson, A. Naumov, S. Fernandez-Alberti, and S. Tretiak, Chemical Physics **481**, 84 (2016).
[20] A. Jain, E. Alguire, and J. E. Subotnik, J. Chem. Theory Comput. **12**, 5256 (2016).
[21] P. L. Walters and N. Makri, J. Chem. Phys. **144**, 044108 (2016).
[22] S. Pal, D. J. Trivedi, A. V. Akimov, B. Aradi, T. Frauenheim, and O. V. Prezhdo, J. Chem. Theory Comput. **12**, 1436 (2016).
[23] S. N. Chowdhury and P. Huo, J. Chem. Phys. **147**, 214109 (2017).
[24] B. F. E. Curchod and T. J. Martinez, Chem. Rev. **118**, 3305 (2018).
[25] R. Crespo-Otero and M. Barbatti, Chem. Rev. **118**, 7026 (2018).
[26] E. Mulvihill, A. Schubert, X. Sun, B. D. Dunietz, and E. Geva, J. Chem. Phys. **150**, 034101 (2019).
[27] S. J. Cotton and W. H. Miller, J. Chem. Phys. **150**, 194110 (2019).
[28] J. E. Runeson and J. O. Richardson, J. Chem. Phys. **152**, 084110 (2020).
[29] J. C. Tully, J. Chem. Phys. **137**, 22A301 (2012).
[30] G. Käb, Phys. Rev. E **66**, 046117 (2002).
[31] P. V. Parandekar and J. C. Tully, J. Chem. Theory Comput. **2**, 229 (2006).
[32] P. Huo and D. F. Coker, Mol. Phys. **110**, 1035 (2012).
[33] R. Lambert and N. Makri, J. Chem. Phys. **137**, 22A552 (2012).
[34] R. Lambert and N. Makri, J. Chem. Phys. **137**, 22A553 (2012).
[35] T. Banerjee and N. Makri, J. Phys. Chem. B **117**, 13357 (2013).
[36] N. Makri, Int. J. Quantum Chem. **115**, 1209 (2015).
[37] C.-Y. Hsieh and R. Kapral, J. Chem. Phys. **137**, 22A507 (2012).
[38] S. J. Cotton, R. Liang, and W. H. Miller, J. Chem. Phys. **147**, 064112 (2017).
[39] S. J. Cotton and W. H. Miller, J. Chem. Phys. **145**, 144108 (2016).
[40] S. J. Cotton and W. H. Miller, J. Chem. Phys. **139**, 234112 (2013).
[41] S. J. Cotton and W. H. Miller, J. Phys. Chem. A **117**, 7190 (2013).
[42] S. J. Cotton and W. H. Miller, J. Chem. Phys. **150**, 104101 (2019).
[43] S. J. Cotton and W. H. Miller, J. Chem. Phys. **150**, 194110 (2019).
[44] J. E. Runeson and J. O. Richardson, J. Chem. Phys. **152**, 084110 (2020).
[45] J. E. Runeson and J. O. Richardson, J. Chem. Phys. **151**, 044119 (2019).
[46] J. R. Mannouch and J. O. Richardson, J. Chem. Phys. **153**, 194109 (2020).
[47] J. R. Mannouch and J. O. Richardson, J. Chem. Phys. **153**, 194110 (2020).
[48] X. He, B. Wu, Z. Gong, and J. Liu, J. Phys. Chem. A **125**, 6845 (2021).
[49] X. He, Z. Gong, B. Wu, and J. Liu, J. Phys. Chem. Lett. **12**, 2496 (2021).
[50] X. He and J. Liu, J. Chem. Phys. **151**, 024105 (2019).
[51] H. Lang, O. Vendrell, and P. Hauke, J. Chem. Phys. **155**, 024111 (2021).
[52] J. R. Mannouch and J. O. Richardson, The Journal of Chemical Physics **158**, 104111 (2023).
[53] J. E. Runeson and D. E. Manolopoulos, The Journal of Chemical Physics **159**, 094115 (2023).
[54] J. R. Mannouch and A. Kelly, (2024), 10.48550/arXiv.2402.07299, arXiv:2402.07299 [physics].
[55] G. Amati, J. R. Mannouch, and J. O. Richardson, "Detailed balance in mixed quantum-classical mapping approaches," (2023), arXiv:2309.04686 [quant-ph].
[56] P. Huo and D. F. Coker, J. Chem. Phys. **135**, 201101 (2011), publisher: American Institute of Physics.
[57] A. Mandal, S. S. Yamijala, and P. Huo, J. Chem. Theory Comput. **14**, 1828 (2018).
[58] A. Mandal, F. A. Shakib, and P. Huo, J. Chem. Phys. **148**, 244102 (2018).
[59] A. Mandal, J. S. Sandoval C., F. A. Shakib, and P. Huo, J. Phys. Chem. A **123**, 2470 (2019).
[60] J. S. Sandoval, A. Mandal, and P. Huo, J. Chem. Phys. **149**, 044115 (2018).
[61] W. Zhou, A. Mandal, and P. Huo, J. Phys. Chem. Lett. **10**, 7062 (2019).
[62] B. M. Weight, A. Mandal, and P. Huo, J. Chem. Phys. **155**, 084106 (2021).
[63] D. Hu, A. Mandal, B. M. Weight, and P. Huo, J. Chem. Phys.

(2022), 10.1063/5.0127118.

[64] Y. Guan, H. Guo, and D. R. Yarkony, J. Chem. Phys. **150**, 214101 (2019).

[65] X. Zhu and D. R. Yarkony, J. Chem. Phys. **137**, 22A511 (2012).

[66] Y. Wang, C. Xie, H. Guo, and D. R. Yarkony, J. Phys. Chem. A **123**, 5231 (2019).

[67] L. M. Ibele and B. F. E. Curchod, Phys. Chem. Chem. Phys. **22**, 15183 (2020), publisher: The Royal Society of Chemistry.

[68] P. Vindel-Zandbergen, L. M. Ibele, J.-K. Ha, S. K. Min, B. F. E. Curchod, and N. T. Maitra, J. Chem. Theory Comput. (2021), 10.1021/acs.jctc.1c00346.

[69] L. M. Ibele, Y. Lassmann, T. J. Martínez, and B. F. E. Curchod, J. Chem. Phys. **154**, 104110 (2021).

[70] A. Mandal, J. S. Sandoval C., F. A. Shakib, and P. Huo, J. Phys. Chem. A **123**, 2470 (2019).

[71] W. Zhou, A. Mandal, and P. Huo, J. Phys. Chem. Lett. **10**, 7062 (2019), publisher: American Chemical Society.

[72] S. Mai, M. Richter, M. Heindl, M. F. S. J. Menger, A. Atkins, M. Ruckenbauer, F. Plasser, L. M. Ibele, S. Kropf, M. Oppel, P. Marquetand, and L. Gonz'alez, "SHARC2.1: Surface Hopping Including Arbitrary Couplings — Program Package for Non-Adiabatic Dynamics," (2019).

[73] H.-J. Werner, P. J. Knowles, G. Knizia, F. R. Manby, and M. Schütz, WIREs Comput Mol Sci **2**, 242 (2012).

[74] J. P. Dahl and M. Springborg, J. Chem. Phys. **88**, 4535 (1988).

[75] R. Schinke, *Photodissociation Dynamics: Spectroscopy and Fragmentation of Small Polyatomic Molecules* (Cambridge University Press, 1995).

[76] D. Tannor, University Science books: Mill Valley, U.S.A (2007).

[77] J. C. Tully, J. Chem. Phys. **93**, 1061 (1990).

[78] G. Granucci, M. Persico, and A. Toniolo, J. Chem. Phys. **114**, 10608 (2001).

[79] J. E. Subotnik and N. Shenvi, J. Chem. Phys. **134**, 024105 (2011).